doi:10.1093/brain/awy126

BRAIN
A JOURNAL OF NEUROLOGY

A novel adeno-associated virus capsid with enhanced neurotropism corrects a lysosomal transmembrane enzyme deficiency

Julie Tordo,[1,*] Claire O'Leary,[2,*] André S. L. M. Antunes,[1] Nuria Palomar,[1] Patrick Aldrin-Kirk,[3] Mark Basche,[4] Antonette Bennett,[5] Zelpha D'Souza,[2] Hélène Gleitz,[2] Annie Godwin,[2] Rebecca J. Holley,[2] Helen Parker,[2] Ai Yin Liao,[2] Paul Rouse,[2] Amir Saam Youshani,[2] Larbi Dridi,[6] Carla Martins,[6] Thierry Levade,[7] Kevin B. Stacey,[8] Daniel M. Davis,[8] Adam Dyer,[1] Nathalie Clément,[9] Tomas Björklund,[3] Robin R. Ali,[4] Mavis Agbandje-McKenna,[5] Ahad A. Rahim,[10] Alexey Pshezhetsky,[6] Simon N. Waddington,[11,12] R. Michael Linden,[1] Brian W. Bigger[2,#] and Els Henckaerts[1,#]

[*,#]These authors contributed equally to this work.

Recombinant adeno-associated viruses (AAVs) are popular *in vivo* gene transfer vehicles. However, vector doses needed to achieve therapeutic effect are high and some target tissues in the central nervous system remain difficult to transduce. Gene therapy trials using AAV for the treatment of neurological disorders have seldom led to demonstrated clinical efficacy. Important contributing factors are low transduction rates and inefficient distribution of the vector. To overcome these hurdles, a variety of capsid engineering methods have been utilized to generate capsids with improved transduction properties. Here we describe an alternative approach to capsid engineering, which draws on the natural evolution of the virus and aims to yield capsids that are better suited to infect human tissues. We generated an AAV capsid to include amino acids that are conserved among natural AAV2 isolates and tested its biodistribution properties in mice and rats. Intriguingly, this novel variant, AAV-TT, demonstrates strong neurotropism in rodents and displays significantly improved distribution throughout the central nervous system as compared to AAV2. Additionally, sub-retinal injections in mice revealed markedly enhanced transduction of photoreceptor cells when compared to AAV2. Importantly, AAV-TT exceeds the distribution abilities of benchmark neurotropic serotypes AAV9 and AAVrh10 in the central nervous system of mice, and is the only virus, when administered at low dose, that is able to correct the neurological phenotype in a mouse model of mucopolysaccharidosis IIIC, a transmembrane enzyme lysosomal storage disease, which requires delivery to every cell for biochemical correction. These data represent unprecedented correction of a lysosomal transmembrane enzyme deficiency in mice and suggest that AAV-TT-based gene therapies may be suitable for treatment of human neurological diseases such as mucopolysaccharidosis IIIC, which is characterized by global neuropathology.

1 Department of Infectious Diseases, School of Immunology and Microbial Sciences, King's College London, London, UK
2 Stem Cell and Neurotherapies, Division of Cell Matrix Biology and Regenerative Medicine, School of Biological Sciences, Faculty of Biology Medicine and Health, University of Manchester, Manchester, UK
3 Molecular Neuromodulation, Wallenberg Neuroscience Center, Lund University, Lund, Sweden
4 Department of Genetics, UCL Institute of Ophthalmology, London, UK
5 Department of Biochemistry and Molecular Biology, Center for Structural Biology, McKnight Brain Institute, College of Medicine, University of Florida, Gainesville, FL, USA
6 CHU Ste-Justine, University of Montreal, Montreal, Canada

Received November 30, 2017. Revised March 19, 2018. Accepted March 21, 2018.

7 Centre Hospitalo-Universitaire de Toulouse, Institut Fédératif de Biologie, Laboratoire de Biochimie Métabolique, and Unité Mixte de Recherche (UMR) 1037 Institut National de la Santé et de la Recherche Médicale (INSERM), Centre de Recherche en Cancérologie de Toulouse, Toulouse, France
8 Manchester Collaborative Centre for Inflammation Research, Division of Infection, Immunity and Respiratory Medicine, School of Biological Sciences, Faculty of Biology Medicine and Health, University of Manchester, Manchester, UK
9 Department of Pediatrics, Powell Gene Therapy Center, University of Florida, Gainesville, FL, USA
10 Department of Pharmacology, UCL School of Pharmacy, University College London, London, UK
11 Gene Transfer Technology Group, Institute for Women's Health, University College London, London, UK
12 Wits/SAMRC Antiviral Gene Therapy Research Unit, Faculty of Health Sciences, University of the Witwatersrand, Johannesburg, South Africa

Correspondence to: Els Henckaerts
Department of Infectious Diseases, School of Immunology and Microbial Sciences, King's College London, London, UK
E-mail: els.henckaerts@kcl.ac.uk

Correspondence may also be addressed to: Brian W. Bigger
Stem Cell and Neurotherapies, Division of Cell Matrix Biology and Regenerative Medicine, School of Biological Sciences, Faculty of Biology Medicine and Health, University of Manchester, Manchester, UK
E-mail: brian.bigger@manchester.ac.uk

Keywords: adeno-associated virus; capsid engineering; neurotropism; mucopolysaccharidosis; lysosomal transmembrane enzyme

Abbreviations: AAV = adeno-associated virus; GlcNS = *N*-sulpho-glucosamine; HS = heparan sulphate; HSPG = heparan sulphate proteoglycan; IgG = immunoglobulin G; MPSIIIC = mucopolysaccharidosis type IIIC; UA = uronic acid

Introduction

Recent clinical trials have demonstrated safety and efficacy of adeno-associated virus (AAV)-mediated gene therapies targeting the eye, muscle and liver (Nathwani *et al.*, 2014; Bainbridge *et al.*, 2015; Russell *et al.*, 2017; Sparks Therapeutics, 2017). However, despite recent unparalleled results in an AAV gene therapy trial for spinal muscular atrophy (Mendell *et al.*, 2017), other AAV gene therapies directed at the brain of patients with rare neurological diseases have shown only limited efficacy (Worgall *et al.*, 2008; Tardieu *et al.*, 2014, 2017). One of the main difficulties associated with gene therapy for CNS diseases is the inefficient AAV distribution to neurons from injection sites in patients. To overcome this hurdle, various strategies have been used to identify or generate more suitable AAV capsids for CNS transduction. These include the discovery of new AAV serotypes in humans and non-human primates and the thorough characterization of their brain tropism (Gao *et al.*, 2002, 2004; Cearley and Wolfe, 2006; Foust *et al.*, 2009; Bevan *et al.*, 2011). Concurrently, diverse capsid engineering strategies emerged as approaches to direct the AAV vectors to defined cell types (Müller *et al.*, 2003; Chen *et al.*, 2009; Adachi *et al.*, 2014). AAV capsids can be improved through rational design, directed evolution techniques and *in vivo* selection in mouse or humanized mouse models (Asokan *et al.*, 2010; Shen *et al.*, 2013; Kotterman and Schaffer, 2014; Lisowski *et al.*, 2014; Tervo *et al.*, 2016; Kanaan *et al.*, 2017). Recently, a novel engineering approach based on *in silico* reconstruction of ancestral viruses has yielded a promising vector for gene therapy of diseases that affect liver, muscle or retina (Zinn *et al.*, 2015). Here we report an alternative evolutionary approach to AAV capsid design based on the introduction of amino acids conserved in AAV2 variants that are currently circulating in the human population (Chen *et al.*, 2005).

This yields a potent neurotropic vector, which may be ideally suited to treat human neurological diseases such as mucopolysaccharidosis type IIIC (MPSIIIC). This disease is caused by mutations in the heparan sulphate acetyl-CoA: α-glucosaminide *N*-acetyltransferase (*HGSNAT*) gene, resulting in a deficiency in the lysosomal enzyme HGSNAT (EC 2.3.1.78). Deficiency of HGSNAT causes progressive accumulation of undegraded heparan sulphate (HS) in all cells of the body (Ruijter *et al.*, 2008). Patients with MPSIIIC have mild visceral manifestations; however, neurological symptoms are severe, characterized by behavioural problems, cognitive decline and, eventually, dementia and death in early adulthood (Ruijter *et al.*, 2008; Valstar *et al.*, 2008). Neuroinflammation and storage of secondary substrates contribute to the pathology of the disease (Archer *et al.*, 2014). The HGSNAT protein is a transmembrane lysosomal *N*-acetyltransferase, and thus enzyme replacement therapy approaches relying on cellular uptake of exogenous enzyme by mannose 6 phosphate receptors that are effective in other lysosomal diseases, cannot be used in this setting. Alternatives, including haematopoietic stem cell transplantation, or gene modification of these cells, also rely on cross-correction and therefore will also most likely prove ineffectual (Durand *et al.*, 2010). The majority of the clinical phenotype is neurological in MPSIIIC, with global neuropathology (Martins *et al.*, 2015), therefore direct transgene delivery to the brain using AAV ensuring distribution to the largest number of cells possible may prove beneficial. This approach has been used in both

preclinical studies and clinical trials for the cross-correctable diseases MPSIIIA (Tardieu *et al.*, 2014; Winner *et al.*, 2016) and MPSIIIB (Ellinwood *et al.*, 2011; Tardieu *et al.*, 2017) caused by deficiencies of soluble secreted enzymes using serotypes rhesus 10 (rh10) and 5, respectively, but even in this case clinical efficacy has been limited. Improved vector distribution in the brain is paramount to overcome these issues, particularly in the case of non-secreted neurological proteins, such as the one deficient in MPSIIIC. Here we present data demonstrating that an alternative approach to capsid engineering, drawing on the natural evolution of the virus, yields a potent neurotropic vector that is more effectively distributed within the brain than the benchmark vectors AAV9 and AAVrh10, and displays an improved ability to correct the neurological phenotype in MPSIIIC mice. The utilization of AAV-TT paves the way for more effective clinical correction of neurological diseases such as MPSIIIC.

Material and methods

AAV-TT model generation

The AAV2-TT monomer model was generated with Swiss-model (https://swissmodel.expasy.org) (Biasini *et al.*, 2014) using the AAV2 crystal structure (RSCB PDB ID no. 1LP3) supplied as a template and the AAV-TT sequence. The AAV-TT VP3 60-mer capsid coordinates were generated by icosahedral matrix multiplication using the Oligomer Generator subroutine available on the VIPERdb online server (http://viperdb.scripps.edu) (Carrillo-Tripp *et al.*, 2009) and visualized by the program Pymol (The PyMOL Molecular Graphics System, Version 1.8 Schrödinger, LLC.).

Animals

Outbred CD1 mice were time mated to produce neonatal animals. Female Sprague Dawley rats (225–250 g) were purchased from Charles River and were housed with free access to food and water under a 12 hour light/dark cycle in a temperature-controlled room. All experimental procedures were approved by the Ethical Committee for Use of Laboratory Animals in the Lund-Malmoü region.

Mice used for ocular injections were female C57Bl/6J mice and were housed at University College London facilities. All animal experiments were conducted according to the ARVO Statement for the Use of Animals for Vision and Ophthalmic Research.

The MPSIIIC mouse model with targeted disruption of the *Hgsnat* gene was generated previously (Martins *et al.*, 2015). MPSIIIC and wild-type mice were maintained at 21 ± 1°C, with a constant humidity of 45–65%, on a 12 h light/dark cycle with *ad libitum* access to food and water. These studies were approved by the Ethics Committee of the University of Manchester. All studies performed on mice were approved by the UK Home Office for the conduct of regulated procedures under license according to the Animals (Scientific Procedures) Act 1986.

Recombinant AAV vector production

The AAV-CAG coHGSNAT transgene plasmid was constructed by replacing the GFP coding sequence in the pTRUF-11 plasmid (ATCC, MBA-331) with a human codon-optimized *HGSNAT* cDNA (including a Kozak sequence) into the SbfI and SphI sites.

Recombinant AAV was produced, purified and titred using standard procedures (Supplementary material). The vectors were titre-matched before injection.

Intracranial injections

Intracranial injections in neonatal mice were carried out as previously described (Kim *et al.*, 2013). Neonatal CD1 mice were prepared for injection by cryoanaesthesia at Day 1 post-gestation (P1) and 5×10^{10} vector genomes (vg) were injected via intracerebroventricular injection in a volume of 5 µl per brain using a 33-gauge needle (Hamilton). The experimental groups existed of equal mixes of male and female animals.

Adult female wild-type rats were injected in the substantia nigra or in the striatum at a dose of 3.5×10^9 vg per injection. Rats were anaesthetized with fentanyl-dormitor (Apoteksbolaget) and placed in the stereotactic frame with the tooth bar individually adjusted for flat skull (bregma-lambda; tooth bar: −3 to −4 mm). A hole was drilled through the skull and the viral vectors were infused unilaterally into the brain. Injections were performed using a pulled glass capillary (60–80 µm internal diameter and 120–160 µm outer diameter) attached to a 25 µl Hamilton syringe connected to an automated infusion pump system. Infusions into the striatum used 3 µl of viral vector preparations at the following coordinates relative to the bregma: antero-posterior (AP) = +0.4; medio-lateral (ML) = −3.5; dorso-ventral (DV) = −5.0/−4.0, with an infusion rate of 0.4 µl/min. Infusion into the ventral midbrain used 3 µl of viral vector at AP = −5.3; ML = −1.7; DV = −7.2, with an infusion rate of 0.2 µl/min. The capillary was left in position for 2 min before retraction.

Eight-week-old female MPSIIIC and wild-type mice were anaesthetized and placed in a stereotactic frame. The stereotactic coordinates used were: striatal, located 2 mm lateral and 3 mm deep to bregma. Using 26-gauge Hamilton syringe, 2.6×10^9 vg/hemisphere were delivered into each striatum at a rate of 0.5 µl/min (3 µl/hemisphere). Sham treated mice received either phosphate-buffered saline (PBS) or AAV-GFP (3 µl/hemisphere). The needle was left in place for 5 min after each infusion before retraction.

Intraocular injections

Intraocular injections were performed under general anaesthesia using an operating microscope (Supplementary material). Six-week-old female mice were injected with viral vectors at a dose of 2×10^9 vg per eye, in a volume of 2 µl per eye, and each mouse received an injection of AAV-TT in one eye and an injection of AAV2 in the contralateral eye.

Tissue preparation

Mice that received vector as neonates were sacrificed at 28 days post-injection by terminal isoflurane anaesthesia followed by exsanguination perfusion with PBS. The brains were removed and fixed for 48 h at 4°C in 4% paraformaldehyde (PFA) and then transferred to 30% sucrose for cryoprotection. Brains were sectioned at −20°C using a cryostat microtome to 40 µm thickness. Sections were stored in anti-freeze buffer (50 mM sodium azide, pH 7.4 containing 25% glycerol and 30% ethylene glycol) at 4°C until use.

Adult rats were sacrificed 28 days post-injection by sodium pentobarbital overdose (Apoteksbolaget) and transcardially perfused with 150 ml PBS followed by 250 ml of ice-cold 4% PFA in 0.1 M phosphate buffer (pH 7.4). The brains were removed and post-fixed for 2 h in ice-cold PFA before storing in 25% buffered sucrose. Brains were cut into coronal sections to 35 µm thickness using a sliding microtome (HM 450, Thermo Scientific). Sections were stored in anti-freeze solution (0.5 M sodium phosphate buffer, 30% glycerol and 30% ethylene glycol) at −20°C until use.

Adult mice were sacrificed 6 weeks after intra-ocular injections. Tissues were fixed in 4% PFA for 1 h and then embedded in O.C.T. medium (R.A. Lamb) and frozen in pre-cooled isopentane. Specimens were stored at −20°C and 18 µm thick sections were cut using a Bright cryostat. Slides were stored at −20°C. Sections were air dried for 10 min before immunostaining.

MPSIIIC and wild-type adult mice were anaesthetized and transcardially perfused with 37°C PBS to remove blood from organs. Samples of liver, lung, kidneys and spleen tissue and one hemisphere of brain were frozen at −80 °C. The other brain hemisphere was fixed in 4% PFA for 24 h then treated with 30% sucrose 2 mmol/l $MgCl_2$/PBS for 48 h before freezing at −80 °C. For HGSNAT assays, brain tissue was dissected into precise hemicoronal fifths (R1–R5). The injection site was in section R2 (rostral to caudal) close to the border of R2/R3. For HS quantification, vector copy number determination and thin-layer chromatography, a full hemisphere was used. For HGSNAT and HS assays, samples were homogenized and sonicated in homogenization buffer (0.5 mol/l NaCl, 0.02 mol/l Tris pH 7–7.5), then centrifuged at 2200*g* for 15 min at 4°C, and the supernatant was collected. Protein concentration was determined using Pierce BCA assay kit (Fisher Scientific). All brain sections were cut from O.C.T. embedded tissues using a freezing microtome.

Immunohistochemical staining

Immunohistochemical staining of neonatal mouse brain sections to detect GFP was performed as previously described (Rahim *et al.*, 2012) using the following antibodies: anti-GFP (1:4000, ab290, Abcam), biotinylated secondary antibody (1:1000, BA-1000, Vector Laboratories) (Supplementary material). Representative images were captured using a live video camera (Nikon, DS-Fil) mounted onto a Nikon Eclipse E600 microscope.

For immunohistochemical analysis in adult rat brains, a standard free-floating protocol was used with an anti-GFP primary antibody (1:20 000, ab13970, Abcam). Biotinylated secondary antibody (1:250, BA-9010, Vector Laboratories) was used for DAB immunohistochemistry and amplified by Vector Labs ABC kit (Supplementary material). Images were captured using an Olympus BX53 microscope and analysed using cellSens Dimension v. 1.11 software.

For Isolectin B4 (ILB4) staining in adult mouse brains, coronal sections (30 µm) were stained as previously described (Wilkinson *et al.*, 2012).

Quantitative analysis of immunohistochemical staining

Levels of GFP immunohistochemical staining were measured by quantitative thresholding image analysis as previously described (Rahim *et al.*, 2012). Data were separately plotted graphically as the mean percentage area of immunoreactivity per field [± standard error of the mean (SEM)].

Immunofluorescence staining and confocal microscopy

For immunofluorescence analysis of neonatal mouse brain sections, the following primary antibodies were used: anti-GFP (1:1000, ab13970, Abcam), anti-calbindin (1:20 000, CB38, Swant), anti-TH; (1:500; AB152, Millipore), anti-GFP (1:4000, ab290, Abcam), anti-ChAT (1:100, AB144P, Millipore), anti-S100β (1:500, ab52642, Abcam). For immunofluorescence, Alexa-conjugated secondary antibodies were used. After washing in TBS, sections were counterstained with DAPI, mounted and coverslipped with Fluoromount G® (SouthernBiotech). Sections were visualized with a laser scanning confocal microscope (Nikon, Eclipse Ti-E Inverted, A1R-Si confocal) and images were processed using NIS Elements and Photoshop software.

Eye sections were counterstained with DAPI using a 5 µg/ml solution in Tris-buffered saline (TBS) for 15 min and coverslipped using Dako mounting medium. Microscopy of specimens was performed using an upright confocal laser scanning microscope (Leica TCS SPE DM5500 Q, Leica Microsystems) and the manufacturer's software (Leica LAS AF, Version 2.4.1). All images presented are confocal *z*-projections through 18 µm sections with DAPI in blue and eGFP in green.

For immunofluorescence staining of 30 µm brain sections from adult wild-type and MPSIIIC mice, the following primary antibodies were used: anti-GFP (1:1000, ab13970, Abcam), anti-NeuN (1:500, ab177487, Abcam), anti-GFAP (1:1500, Z-0334, Dako), anti-LAMP2 (1:200, ab13524, Abcam). Alexa-conjugated secondary antibodies were used. Sections were mounted using ProLong® Gold Antifade medium with DAPI (Life Technologies). Images were acquired on a 3D-Histech Pannoramic-250 microscope slide-scanner using a 20×/0.30 Plan Achromat objective (Zeiss) and the DAPI, FITC and TRITC filter sets and processed using Case Viewer software (3D-Histech). GFP immunofluorescence was visualized at ×100 on a confocal laser scanning microscope (Leica TCS SP8).

For analysis of G_{M2} and G_{M3} gangliosides, 40 µm sagittal brain sections were incubated with anti-G_{M2} (KM966, 1:500) or anti-G_{M3} (M2590, Cosmo Bio Co., Ltd., 1:100). Alexa-conjugated secondary antibodies and Draq5™ solution (ThermoFisher Scientific) were used. Sections were mounted using Vectashield® medium. The images were first analysed at low magnification using Zeiss Slide Scanner Axio Scan.Z1 (10×/0.45) for G_{M2} staining and Nikon Eclipse E800 fluorescence microscope (5×) for G_{M3} staining.

For quantification of G_{M2} ganglioside, images were acquired using a LSM510 Meta Laser inverted confocal microscope (Zeiss, 20×/0.4) or a Leica TCS SPE confocal microscope (10×/0.3). Quantification of immunofluorescence was assessed by ImageJ software (National Institutes of Health, Bethesda, MD, USA).

Quantification of NeuN/GFP co-localization

To demonstrate that GFP was primarily located within neurons, automated counting was performed using the analyse particles plugin in FIJI. NeuN/GFP double positive cells were counted using FIJI in a representative 40× section for each brain area ($n = 4$ individual mice/group).

HGSNAT enzyme assay

HGSNAT enzyme activity was measured using 4-methylumbelliferyl-β-D-*N*-glucosaminide (MU-βGlcNH2, Moscerdam) as a substrate (Supplementary material).

Open-field behaviour

Open field behaviour was analysed as previously described (Langford-Smith *et al.*, 2011; Martins *et al.*, 2015). Outliers were removed using the Tukey outlier method of 1.5× interquartile range (IQR).

Spontaneous alternation

Spontaneous alternation was assessed during one continuous 10-min session in a Y-maze consisting of three identical arms as previously described (O'Leary *et al.*, 2014). All animals fell within the minimal 33% alternation for outlier identification.

Indirect enzyme-linked immunosorbent assay detection of anti-AAV IgG antibodies

Total IgG antibody responses against AAV capsid proteins were measured with an enzyme-linked immunosorbent assay (ELISA) assay, using several brain homogenate dilutions, biotinylated goat anti-mouse IgG antibody (Vector) and the Vectastain ABC kit (Vector) (Supplementary material).

Vector copy number determination

Analysis of vector biodistribution was performed by quantitative PCR (qPCR) (Supplementary material).

Analysis of brain gangliosides by thin-layer chromatography

Briefly, frozen brain tissues were homogenized in water (10% v/w) using a FastPrep-24 MP homogenizer. Lipids were extracted by addition of two volumes of methanol and one volume of chloroform to one volume of the homogenate. After 10 min centrifugation at 1000*g* the organic phase was collected, and used to analyse gangliosides by phase separation as previously described (Seyrantepe *et al.*, 2008).

Glycosaminoglycan analysis

Glycosaminoglycan chains were purified, 2-aminoacridone (AMAC)-labelled and analysed by reversed-phase high-performance liquid chromatography (RP-HPLC) as previously described (Holley, 2018).

Statistical analysis

Statistical analysis was performed using Graphpad Prism software. All data were analysed by either Student's *t*-tests or ANOVA and Tukey and Sidak's *post hoc* test for analysis. Where standard deviations (SDs) were unequal, data were log transformed to achieve normal distributions. Significance was determined as $P < 0.05$. All the test results are given as exact values, with confidence intervals in the main text.

Experimental design

The MPSIIIC mice treated showed no phenotype at treatment age. The treatment groups were randomly assigned at weaning. MPSIIIC *n*-numbers were based on previous power calculations for biochemical and histological changes as seen in the MPSIIIA mouse model (Sergijenko *et al.*, 2013) and behavioural changes in the MPSIIIB mouse model (Langford-Smith *et al.*, 2011). It was impossible to

blind treatment groups because of the nature of the treatments and the size of the experiment, with treatments staggered over several months. Analysis was carried out in a blinded fashion for biochemical, histological and behavioural analyses. The nature of the analyses was such that unconscious bias is difficult to introduce in any case, as automated quantification methods were used for the most part. Data exclusion: outliers were removed from open field behaviour using the Tukey outlier method of 1.5 × IQR. No other mice were removed from any analysis.

Results

Engineering of a novel AAV2 capsid

We substituted 14 amino acids in the AAV2 capsid gene to create a novel vector, designated AAV-TT, based on the conserved amino acid changes present in natural AAV2 isolates sampled from human paediatric tissues (Chen *et al.*, 2005). These were one amino acid change in the VP1 unique region (VP1u), two in the VP1/VP2 common region, and 11 in VP3 (Fig. 1A). Most notably, arginine (R) at positions 585 and 588 was substituted to serine (S) and threonine (T), respectively (Fig. 1A and B). These changes have been previously shown to abolish heparan sulphate proteoglycan (HSPG) binding (Grifman *et al.*, 2001; Kern *et al.*, 2003; Opie *et al.*, 2003). The majority of substitutions in VP3 are located on the AAV2 capsid surface and cluster around the icosahedral 3-fold axis (Fig. 1C and D). Ribbon diagrams show that most of the substituted amino acids within the structurally ordered VP3 region localize to variable regions IV–VIII (Fig. 1C and E–G), which are involved in receptor binding and determine the antigenic properties of AAV capsids (Gurda *et al.*, 2013; Tseng *et al.*, 2015). To characterize the physical properties of the AAV-TT capsid, its stability was determined by differential scanning fluorimetry (DSF). The melting temperature of AAV-TT is 7°C greater than AAV2 (Supplementary Fig. 1A and B); the melting temperature of AAV2 is consistent with previous reports (Rayaprolu *et al.*, 2013). A recent publication reported that AAV capsid stability has no correlation to AAV1, AAV2, or AAV5 transduction in HEK293 cells and that the stability of the virus is determined by its pI (Bennett *et al.*, 2017). This implies that the increased melting temperature of AAV-TT compared to AAV2 is based on the difference in the number of charged residues between the two viruses.

AAVs have been shown to use different proteoglycans as their primary receptors. AAV-TT exhibits a high sequence homology to AAV2 and AAV3, serotypes that are both dependent on HSPG binding for viral uptake *in vitro* (Summerford and Samulski, 1998). Recombinant AAV-TT and AAV2 were assessed for their ability to transduce various cell lines *in vitro*. Not surprisingly, AAV-TT displayed a lower transduction efficiency than AAV2 and the efficiency of transduction of AAV-TT varied significantly depending on the cell type transduced [effect of treatment, $F(7,13) = 15.82$, $P < 0.0001$] (Supplementary Fig. 2A). The independence of HSPG binding of AAV-TT was further confirmed in a cell-based heparin competition assay showing that AAV-TT transduction efficiency *in vitro* is not affected by the presence of heparin [effect of treatment × vector type, $F(5,24) = 4.047$, $P < 0.01$] (Supplementary Fig. 2B); this was further substantiated by a heparin column-binding assay. Virus-like particles were assembled from AAV5, AAV2 or AAV-TT capsid proteins and were loaded in excess on a heparin column (Supplementary Fig. 2C). AAV2 virus-like particles bind the heparin column and elute with increasing NaCl concentrations, AAV5 virus-like particles flow through the column without binding to heparin and none were further eluted when high concentrations of NaCl were applied. AAV-TT virus-like particles showed a similar profile to AAV5 and were only detected in the flow-through and the wash fractions. These data confirm that AAV-TT capsids do not interact with heparin.

AAV-TT enables widespread transduction in neonatal and adult rodent brains

Prompted by previous reports that high levels of HSPG expression in the brain parenchyma limit vector spread (Nguyen *et al.*, 2001; Mastakov *et al.*, 2002; Kanaan *et al.*, 2017), we assessed AAV-TT's potential for an increased ability to spread in the brain. GFP reporter viruses were delivered via unilateral intracerebroventricular administration [5×10^{10} vector genomes (vg) total] in neonatal mice and biodistribution was assessed using GFP immunohistochemistry. Figure 2A–C shows that increased transduction levels were observed with AAV-TT as compared to AAV2 in the majority of brain sections analysed; quantification of GFP expression in the striatum highlights the strongly enhanced transduction capacity of AAV-TT (two-tailed Student's *t*-test; $t = 13.88$ $df = 4$, $P < 0.001$). Further analysis of the tissues by immunofluorescence microscopy demonstrates that both glial and neuronal cells are targeted by AAV-TT (Fig. 2D and E). The improved *in vivo* transduction profile was further confirmed in adult rats where intrastriatal (Fig. 3A and B) as well as nigral injections of 3.5×10^9 vg (Supplementary Fig. 3A and B) of AAV-TT result in markedly enhanced transduction throughout the hemisphere, whereas the delivery of AAV2 leads to transduction of a small area of cells situated along the needle track. Delivery of AAV-TT into the striatum appears to mediate transduction across the corpus callosum into the cortex, into the intralaminar nuclei of the thalamus, and into the substantia nigra pars compacta (Fig. 3A). All these regions have afferents to the striatum (Fig. 3B), suggesting that retrograde transport may be occurring (Salegio *et al.*, 2013).

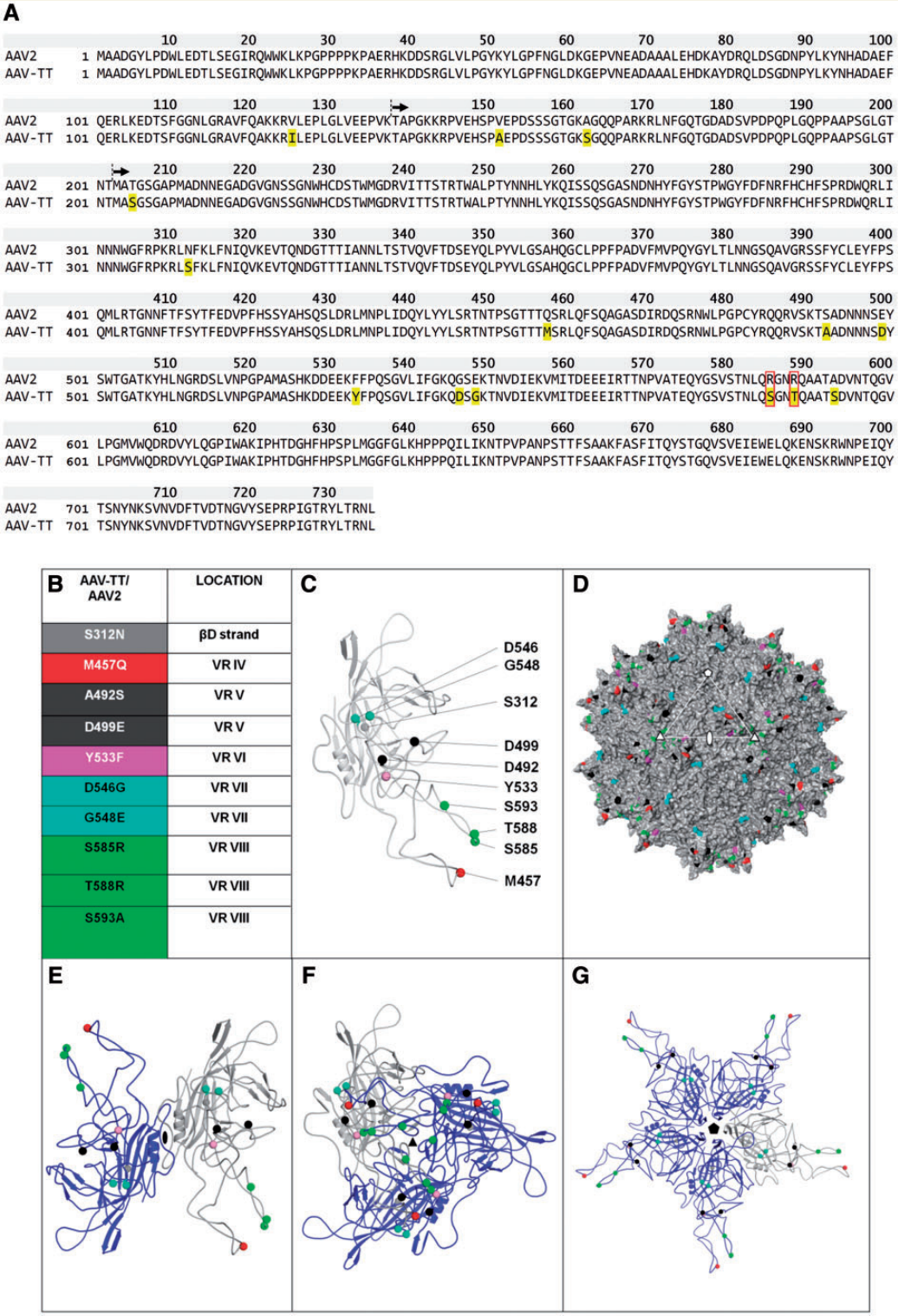

Figure 1 AAV-TT capsid sequence and 3D model. (**A**) Protein alignment of AAV-TT and AAV2 (NCBI, accession number: NC_001401.2). VP1 is shown, with residues in yellow highlighting the amino acids that differ between the two capsids. Residues boxed in red correspond to the amino acid belonging to the basic patch that constitutes the HSPG binding site. Black arrows indicate the start sites of the VP2 and VP3 capsid proteins. (**B**) List of AAV-TT/AAV2 differing residues located in VP3 (the amino acid change at position 205 in AAV-TT is not listed as the 3D structure of the N-terminal end of VP3 is currently unknown). The positions of these residues within VP3 variable regions (VR) are indicated. (**C**) Ribbon diagram of VP3 monomer with AAV-TT/AAV2 differing residues shown as spheres and coloured according to list in **B**. (**D**) Surface representation of the 3D structure of AAV2 VP3 with the position of the residues which differ from AAV-TT coloured as in **B**. The icosahedral 2-, 3-, and 5-fold axes are indicated by an oval, triangle and pentagon, respectively. (**E**–**G**) Ribbon diagrams of VP3 dimer, trimer and pentamer with the reference monomer coloured grey and the symmetry related monomers coloured blue.

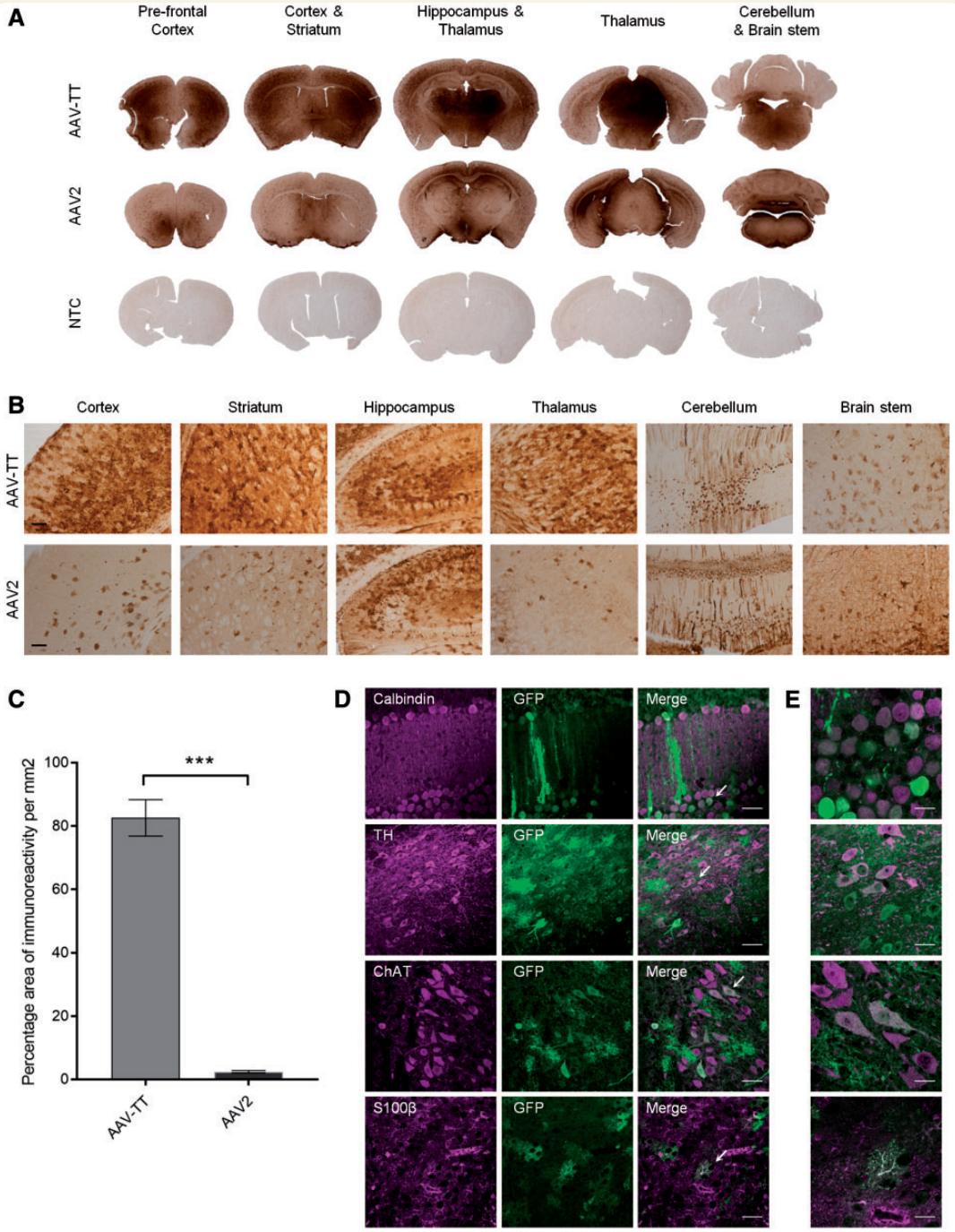

Figure 2 Intracerebroventricular injections in neonatal mice show superior transduction ability of AAV-TT across the CNS. 5×10^{10} vg of GFP-expressing AAV-TT or AAV2 vectors were injected unilaterally into the lateral ventricle of neonatal mice at postnatal Day 1 (P1) ($n = 3$ per condition). (**A**) Representative images of GFP signal observed 4 weeks post-injection in the different brain areas indicated. Brain sections derived from an untreated animal were used as negative control (NTC, non-transduced control, $n = 3$). (**B**) High magnification images of the sections shown in **A**. Scale bar = 100 μm. (**C**) GFP signal quantified as the percentage area of immunoreactivity measured in the striatum of the injected hemisphere. Signal was significantly higher in AAV-TT as compared to AAV2 treated animals. Unpaired Student's *t*-test, two-tailed, $n = 3$ per group. The data are presented as mean ± SEM; $^{***}P < 0.001$. (**D**) Representative images of native GFP fluorescence and calbindin, tyrosine hydroxylase (TH), choline acetyltransferase (ChAT) or S100β taken at 40× magnification show that AAV-TT has the ability to transduce Purkinje cells, dopaminergic neurons, cholinergic neurons and astrocytes respectively. Scale bars = 50 μm. White arrows indicate the areas magnified in **E**. (**E**) Representative images taken at 100× magnification showing GFP expression in the areas indicated by white arrows in the corresponding panels in **D**. Scale bars = 20 μm.

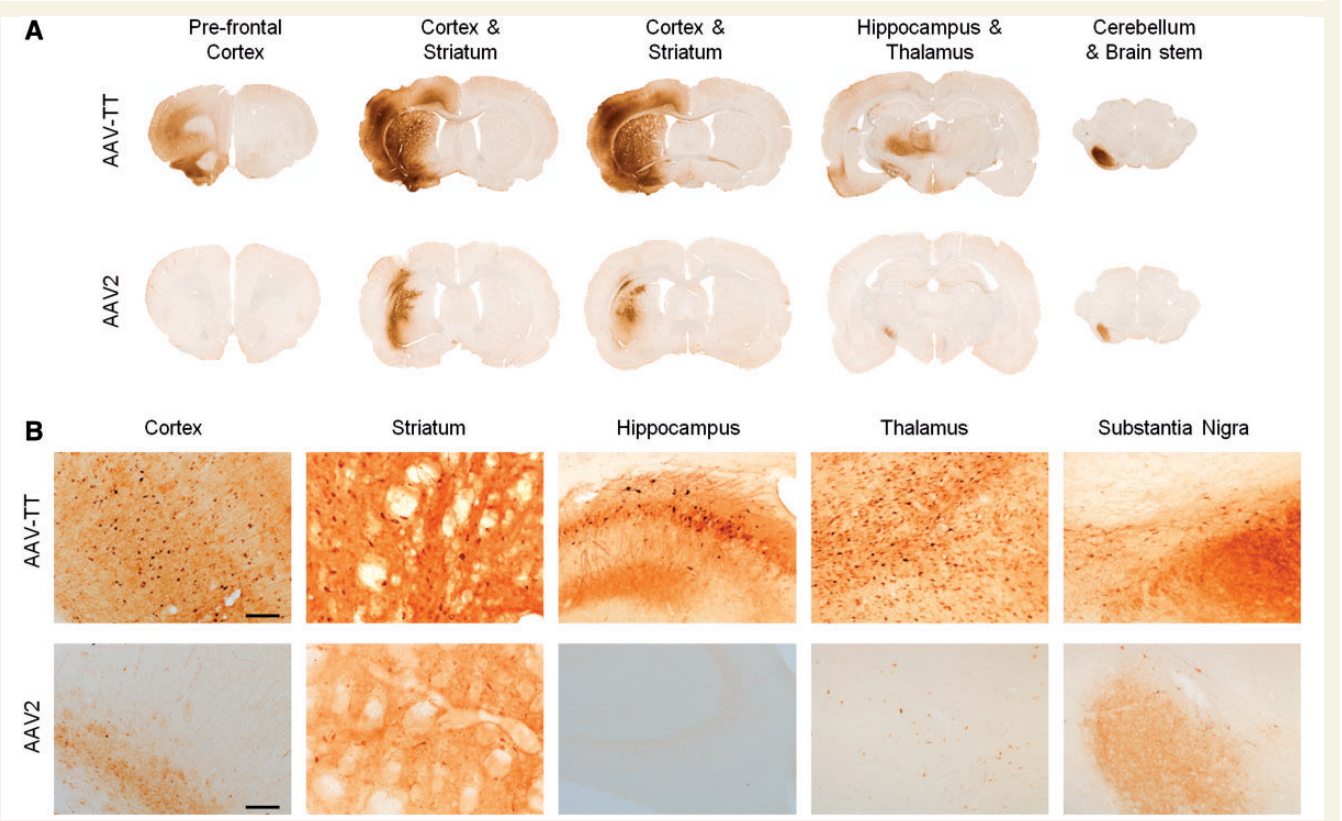

Figure 3 Intrastriatal injections in adult rats show superior transduction ability and vector spread of AAV-TT across large areas of the CNS. GFP-expressing AAV-TT or AAV2 (both 3.5×10^9 vg) were injected into the striatum of adult rat brains ($n = 3$). (**A**) Representative images of GFP signal 4 weeks post-injection in the different brain areas indicated. (**B**) High magnification images of the sections shown in **A**. Scale bar = 100 μm.

AAV-TT efficiently transduces photoreceptors

Given the ability of AAV-TT to target various neuronal cell types, we investigated if this new capsid would show improved transduction of photoreceptors. AAV2 has been used to treat a number of hereditary diseases of the eye that cause blindness, with clinical trials showing improved visual acuity for several years post-treatment (Ripamonti *et al.*, 2015; Russell *et al.*, 2017). However, this serotype has now been eclipsed by a number of other serotypes that have shown improved photoreceptor tropism in preclinical animal studies (Vandenberghe and Auricchio, 2012; Georgiadis *et al.*, 2016). Sub-retinal injections in mice of AAV-TT (2×10^9 vg) and AAV2 (2×10^9 vg, contralateral eye) allowed for side-to-side comparison of both capsid variants; confocal microscopy of transverse sections of the eye showed that AAV-TT has a strongly improved ability to transduce photoreceptors as compared to AAV2. AAV-TT transduced retinal pigment epithelium at least as well as AAV2 (Fig. 4A). Conversely, AAV-TT vectors administered via intravitreal injection showed decreased transduction abilities (Fig. 4B), in line with previous observations that HSPG binding is required for transduction of the retina via this injection route (Boye *et al.*, 2016; Woodard *et al.*, 2016).

In summary, our data show that the introduction of a select number of specific mutations in the AAV2 capsid results in a potent neurotropic vector that could be used to treat diseases of the eye as well as therapeutically more challenging neurological diseases, such as MPSIII, which would benefit by provision of more effective CNS transduction.

AAV-TT exceeds the transduction abilities of AAV9 and AAVrh10 in adult mouse brains

Many AAV serotypes have previously been assessed for their CNS transduction properties in rodents and have shown different expression patterns in the brain (Burger *et al.*, 2004; Cearley and Wolfe, 2006; Klein *et al.*, 2006, 2008; Foust *et al.*, 2009). In preparation for preclinical studies, intracerebral injection of GFP reporter virus of AAV-TT was assessed against AAV serotypes AAV9 and AAVrh10, which had shown particularly good transduction capabilities within the CNS in these studies. For each serotype, relatively low but equivalent viral titres were injected

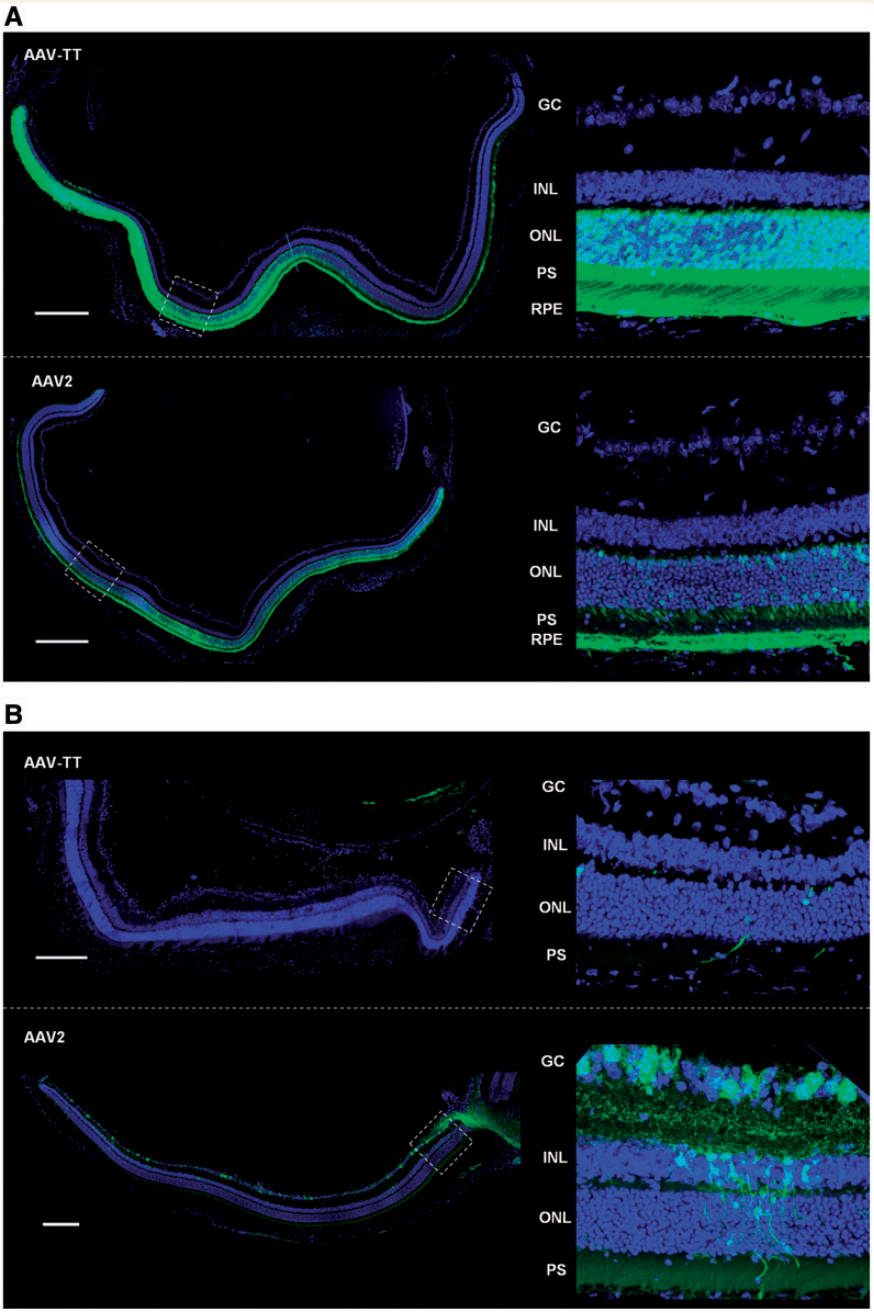

Figure 4 Sub-retinal injections in adult mice show superior transduction ability of AAV-TT throughout different layers of the retina. GFP expressing AAV2 and AAV-TT were injected contralaterally in adult mice at a dose of 2×10^9 vg per eye ($n = 4$ per condition). (**A**) Representative confocal z-projections of transverse sections of the retina taken 4 weeks after sub-retinal injections show that AAV-TT targets a higher number of RPE and photoreceptor cells and mediates increased transgene expression as compared to AAV2. (**B**) AAV-TT cannot efficiently penetrate the retina when injected via the intra-vitreal route; intra-vitreal injection of AAV2 leads to transduction of retinal ganglion cells. GC = ganglion cell layer; INL = inner nuclear layer; ONL = outer nuclear layer; PS = photoreceptor segments; RPE = retinal pigment epithelium. Scale bar = 200 μm.

bilaterally into the caudate putamen of adult mouse brains (2.6×10^9 vg/hemisphere) and GFP expression assessed after 3 weeks (Fig. 5A–C). AAV-TT resulted in greater global transduction of cells throughout the brain compared to either AAV9 or AAVrh10; in which spread of vector was limited to areas within the caudate putamen and thalamus (Fig. 5D). AAV9 gave intense staining in the areas close to the injection site, especially around the needle track (Fig. 5A and D) with limited distribution in other areas. In contrast, GFP expression of AAV-TT was less intense than AAV9 and AAVrh10 but more widely distributed in the brain resulting in a greater number of areas transduced; including the cingulate cortex, thalamus, amygdala, hippocampus, somatosensory cortex and the external capsule,

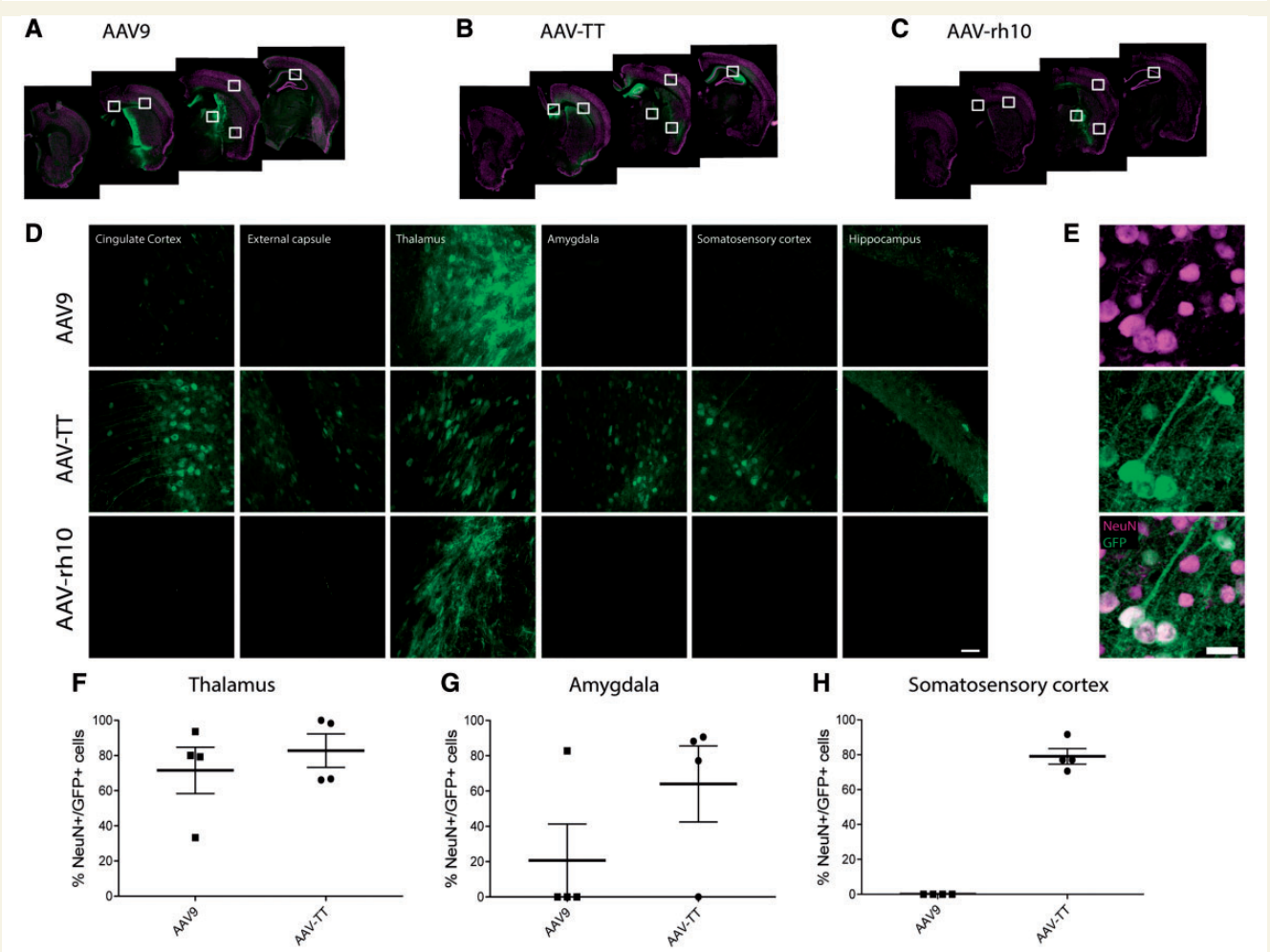

Figure 5 AAV-TT outperforms AAV9 and AAVrh10 in GFP biodistribution studies. GFP vectors were packaged into AAV9, AAVrh10 or AAV-TT capsids and used for comparative biodistribution studies. (**A**–**C**) Representative confocal microscopy images showing GFP expression in the CNS of mice 3 weeks after they were injected with the three different marker viruses. The white squares indicate the areas that are shown at higher magnification in **D**. (**D**) Representative confocal images showing GFP expression in the areas indicated in (**A**–**C**). Scale bar = 50 μm. (**E**) NeuN staining of brain sections of adult mice treated with AAV-TT shows that AAV-TT specifically transduces neurons. Scale bar = 20 μm. The percentage of NeuN/GFP co-localizing cells in the (**F**) thalamus (**G**) amygdala and (**H**) somatosensory cortex in AAV9- and AAV-TT-treated mice.

respectively (Fig. 5B and D). GFP expression was exclusively seen in neurons with expression in both the soma and processes (Fig. 5E). We could not detect GFP in GFAP+ astrocytes or Iba1+ microglia/macrophages (Supplementary Fig. 4A and B). The percentages of GFP/NeuN double positive cells were similar for AAV-TT and AAV9 serotypes in the thalamus, an area close to the injection site (Fig. 5F). However, in areas further away from the injection site such as the amygdala and somatosensory cortex, the percentage of GFP/NeuN double positive cells was markedly higher in AAV-TT-treated mice compared to AAV9-treated mice (Fig. 5G and H). We subsequently compared the therapeutic efficacy of AAV vectors expressing the codon optimized human *HGSNAT* (coHGSNAT) transgene using the two best performing serotypes; AAV9 and AAV-TT.

Relative HGSNAT activity measured in transiently transfected HEK293T cells with a plasmid containing coHGSNAT confirmed that increased HGSNAT enzyme activity was detected intracellularly but not in the supernatant, thereby confirming that the enzyme cannot be secreted [effect of treatment, $F(5,15) = 66.75$, $P < 0.0001$] (Supplementary Fig. 5B).

AAV-TT, but not AAV9 corrects pathological behaviour in MPSIIIC mice

Four months after bilateral intracranial injections (2.6×10^9 vg/hemisphere) of coHGSNAT expressing AAV9 and AAV-TT vectors into MPSIIIC mice, we measured behavioural outcomes; biochemical and histological outcomes were measured 6 months post-treatment (Fig. 6A–C).

MPSIIIC mice have a hyperactive phenotype in the 1 h open field test (Martins *et al.*, 2015) (Fig. 6D). The hyperactive phenotype, assessed by total distance moved was

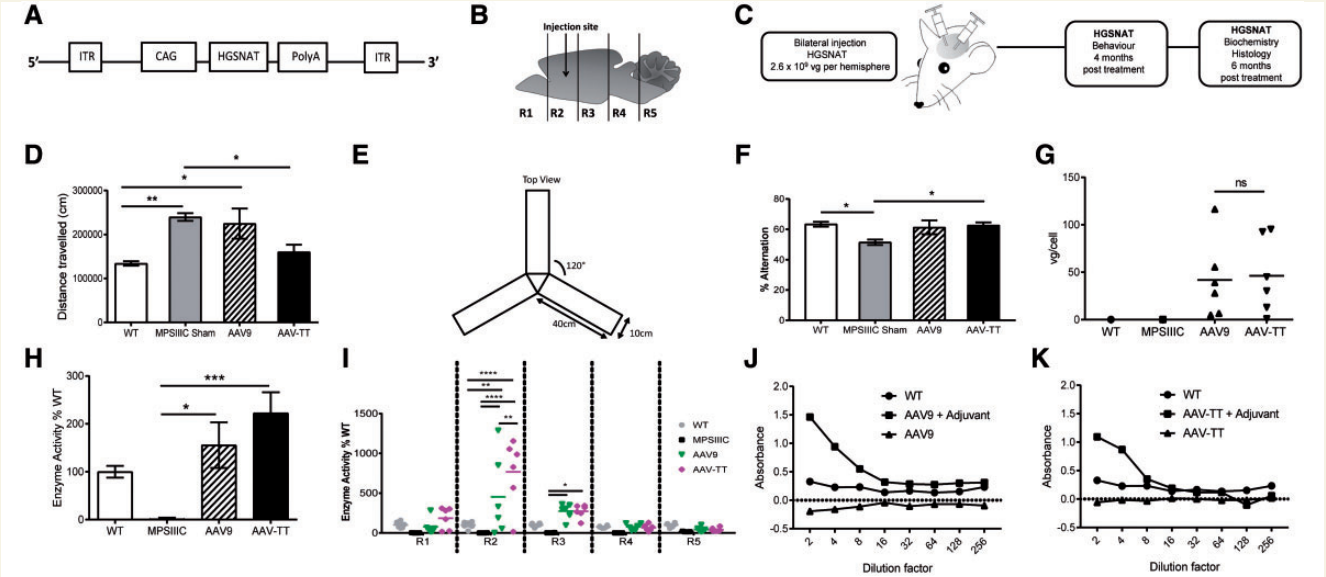

Figure 6 AAV-TT effectively corrects disease phenotype in MPSIIIC mice. (**A**) AAV-HGSNAT vectors, packaged into AAV9 or AAV-TT capsids, were used to treat MPSIIIC mice. (**B**) Schematic of injection site and brain sectioning used for enzyme level determination. (**C**) Overview of treatment and analysis scheme. (**D**) Hyperactivity as measured by distance travelled by wild-type (wt, $n = 8$) and MPSIIIC sham ($n = 11$), AAV9 ($n = 8$) and AAV-TT ($n = 7$) treated MPSIIIC mice. (**E**) Configuration of Y-maze. (**F**) Cognitive ability as measured by the percentage of alternation in the Y- maze of wild-type ($n = 10$) and MPSIIIC sham ($n = 12$), AAV9 ($n = 9$) and AAV-TT ($n = 9$) treated MPSIIIC mice. (**G**) Vector genome copy numbers (vg/cell) measured by qPCR in whole brain tissue preparations from wild-type ($n = 1$), MPSIIIC ($n = 1$), AAV9 ($n = 6$) and AAV-TT ($n = 6$) treated MPSIIIC mice. (**H**) HGSNAT enzyme activity measured in whole brain preparations of wild-type ($n = 6$), MPSIIIC ($n = 6$), AAV9 ($n = 6$) and AAV-TT ($n = 6$) treated MPSIIIC mice. (**I**) HGSNAT enzyme activity measured in brain sections R1–R5. (**J**) Total IgG antibody responses against AAV9 capsid proteins as measured by ELISA. Absence of capsid-specific antibodies in brain homogenates of AAV9-coHGSNAT ($n = 6$) treated mice. (**K**) Total IgG antibody responses against AAV-TT capsid proteins as measured by ELISA. Absence of capsid-specific antibodies in brain homogenates of AAV-TT-HGSNAT ($n = 6$) treated mice. Positive controls consist of mice treated with vectors and adjuvant. ANOVA followed by Tukey's *post hoc* multiple comparison test. Data are presented as mean ± SEM; $^{*}P < 0.05$; $^{**}P < 0.01$; $^{***}P < 0.001$; $^{****}P < 0.0001$.

corrected in AAV-TT treated MPSIIIC mice at 4 months post-treatment, but not in AAV9-treated mice [effect of treatment, $F(3,30) = 7.68$, $P < 0.001$] (Fig. 6D). Impaired cognitive abilities in MPSIIIC mice can be evaluated by assessing working memory as determined by the number of correct entries into the different arms of a Y-maze (Hughes, 2004) (Fig. 6E). This spontaneous alternation task takes advantage of the natural tendency for the mouse to explore novel environments; measurement of working memory in this task consists of an increase in exploration of a novel arm compared to a recently explored arm of the maze (Deacon *et al.*, 2002). Consistent with correction of hyperactivity, AAV-TT treated mice showed significant improvements in immediate spatial working memory and correction to wild-type levels in the Y-maze [effect of treatment, $F(3,35) = 3.806$, $P < 0.05$] (Fig. 6F). AAV9 had a more variable effect that was not significantly improved over MPSIIIC sham.

No statistically significant differences in vector copy numbers in the brain were found among the groups with average numbers of 39.15 ± 16.91 and 45.09 ± 16.29 for AAV9 and AAV-TT, respectively (Fig. 6G). Little to no off-target transduction of AAV9 and AAV-TT to peripheral organs was observed in treated mice with vg/cell values generally under 0.5 vg/cell (Supplementary Fig. 6A, C, E and G). Consistent with vector genome results, no HGSNAT enzyme was detected in spleen, lung and kidney, in all treated animals (Supplementary Fig. 6B, D, F and H).

AAV-TT further improves brain-specific HGSNAT activity at 6 months in MPSIIIC mice

At 6 months post-treatment, AAV-TT and AAV9 vectors expressing coHGSNAT increased overall brain enzyme activity levels to above wild-type levels [effect of treatment, $F(3,97) = 14.19$, $P < 0.0001$]; but higher levels were obtained in AAV-TT (266.5%) treated mice compared to AAV9-treated mice (185.2%) (Fig. 6H). The brain was divided into hemicoronal fifths (anterior to posterior R1–R5; Fig. 6B), with enzyme activity detected throughout the brain but highest around the injection site in R2 [effect of treatment × brain region, $F(12,97) = 4.91$, $P < 0.0001$] (Fig. 6I). In contrast to earlier observations at 1 week and 3 weeks post-treatment (Supplementary Fig. 5C and D), enzyme levels mediated by AAV-TT at 6 months post-treatment were significantly greater than AAV9

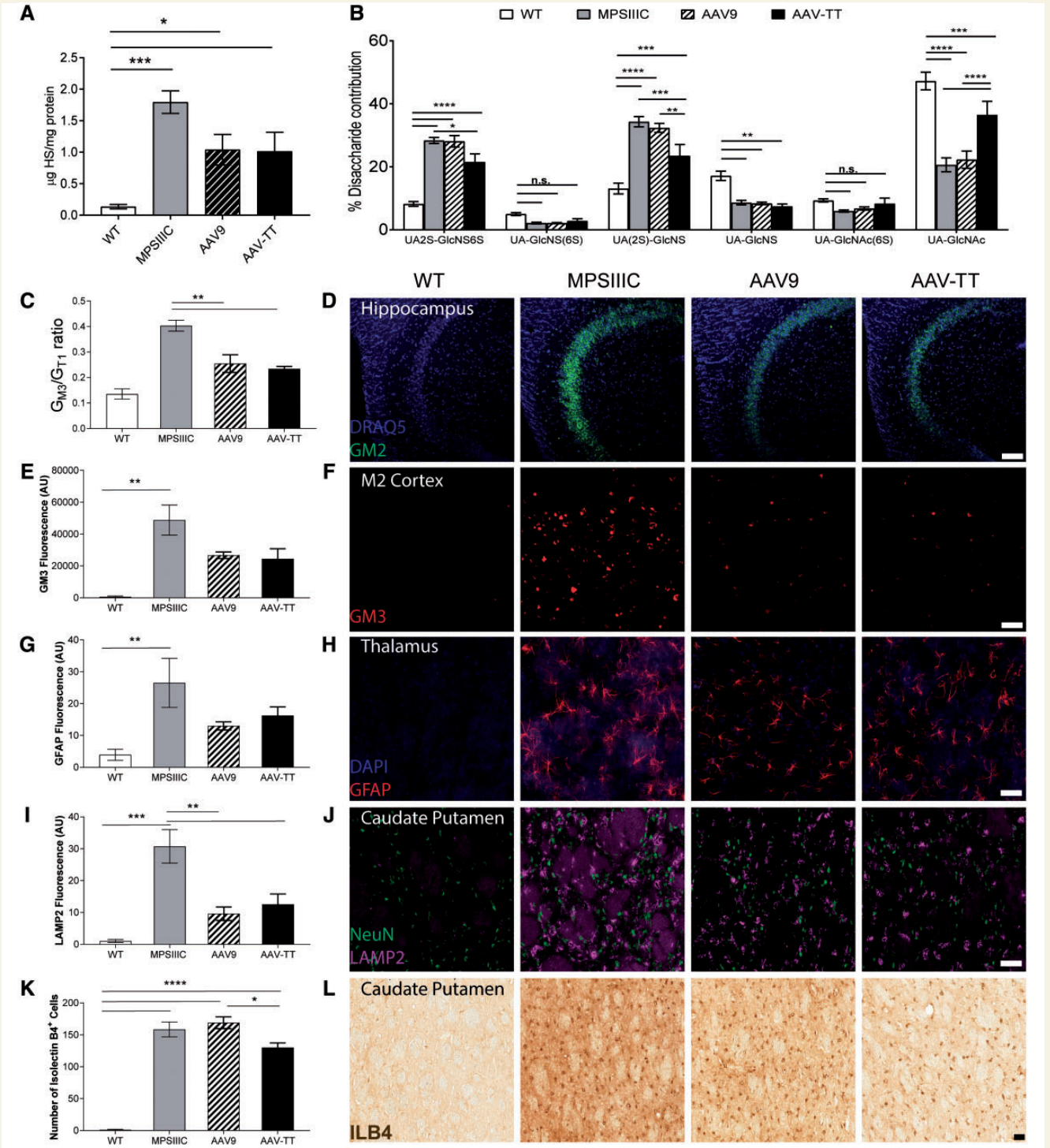

Figure 7 AAV-TT reduces primary and secondary storage molecules leading to a reduction in neuroinflammation in MPSIIIC mice. (**A**) Primary storage i.e. total HS measured by reversed phase chromatography in brains in wild-type (wt, *n* = 6), untreated MPSIIIC (*n* = 6), AAV9 (*n* = 6) and AAV-TT (*n* = 6) treated MPSIIIC mice. (**B**) Measurement of the different disaccharide contributions in HS in wild-type (*n* = 6), untreated MPSIIIC (*n* = 6), AAV9 (*n* = 6) and AAV-TT (*n* = 6) treated MPSIIIC mice shows normalization of the relative proportion of HS that is NAc, 6S and 2S sulphated. (**C**) Secondary storage i.e. G_{M3} gangliosides measured by thin layer chromatography in homogenized brain tissues of wild-type (*n* = 4), untreated MPSIIIC (*n* = 3), AAV9 (*n* = 4) and AAV-TT (*n* = 4) treated MPSIIIC mice, which is reduced in treated MPSIIIC mice. (**D**) Storage of G_{M2} ganglioside in the hippocampus of wild-type (*n* = 2), untreated MPSIIIC (*n* = 6), AAV9 (*n* = 3) and AAV-TT (*n* = 4) treated MPSIIIC mice, which is reduced in treated MPSIIIC mice. (**E** and **F**) Storage of G_{M3} stained brain sections in the M2 cortex of wild-type (*n* = 2), untreated MPSIIIC (*n* = 6), AAV9 (*n* = 3) and AAV-TT (*n* = 4), which is reduced in treated MPSIIIC mice. Scale bar = 20 μm. (**G** and **H**) Confocal microscopy of GFAP stained brain sections in wild-type (*n* = 4), untreated MPSIIIC (*n* = 3), AAV9 (*n* = 4) and AAV-TT (*n* = 4) treated MPSIIIC mice shows trend towards reduction in the accumulation of GFAP positive astrocytes in the thalamus of treated MPSIIIC mice. (**I** and **J**) Confocal

(continued)

($P < 0.001$) in R2 at 767.78% and 453.03%, respectively (Fig. 6I). Despite supra-physiological enzyme levels in treated brains, both AAV9 (Fig. 6J) and AAV-TT (Fig. 6K) capsids produced no detectable levels of anti-AAV IgG antibodies in the brains of all treated mice, in contrast to positive control mice that received a mixture of adjuvant and either AAV9 or AAV-TT to stimulate significant IgG responses.

AAV-TT and AAV9 reduce primary storage of heparan sulphate, while AAV-TT improves heparan sulphate patterning *in vivo*

MPSIIIC mice display a 13.4-fold increase in primary storage of HS in the brain compared to wild-type (Fig. 7A). Overall, AAV9 and AAV-TT both reduced total HS levels by ~46% [effect of treatment, $F(3,20) = 10.03$, $P < 0.001$].

Abnormal highly sulphated UA(2S)-GlcNS(6S) ($P < 0.0001$) and UA(2S)-GlcNS ($P < 0.0001$) HS species were seen in the brains of MPSIIIC mice; with a reduction in the un-sulphated UA-*N*-acetyl-glucosamine (GlcNAc) ($P < 0.0001$) groups. AAV-TT reduced UA(2S)-GlcNS(6S) residues compared to MPSIIIC ($P < 0.01$), whereas levels in AAV9 treated mice remained unchanged. AAV-TT was significantly better at correcting abnormal UA(2S)-GlcNS ($P < 0.01$) and UA-GlcNAc ($P < 0.0001$) disaccharide composition than AAV9 (Fig. 7B).

AAV-TT and AAV9 reduce secondary storage of G_{M2} and G_{M3} gangliosides in the brain of MPSIIIC mice

It has been previously reported that both G_{M3} and G_{M2} gangliosides are significantly increased in the brains of MPSIIIC mice (Martins *et al.*, 2015).

G_{M3} storage is observed (in the order of storage level) in the hypothalamus, amygdala, midbrain, medial entorhinal cortex (MEnt), secondary motor cortex (M2), secondary visual cortex mediolateral, and hippocampus including the molecular layer of the dentate gyrus. AAV treatment with both serotypes significantly reduced overall levels of GM_3 gangliosides in the brains of MPSIIIC mice at 6 months post-injection ($P < 0.01$) (Fig. 7C) including the secondary motor cortex (M2) (Fig. 7E and F) and the medial entorhinal cortex (Supplementary Fig. 7B).

G_{M2} ganglioside levels are abnormally elevated throughout the MPSIIIC brain but particularly (in the order of storage level) in the amygdala, pons, medulla, midbrain, hypothalamus, reticular nucleus of the thalamus, medial entorhinal cortex, cortex, hippocampus and cerebellum. These were reduced in the hippocampus in both groups of treated mice compared to untreated mice (Fig. 7D) and appear reduced in other brain areas (Supplementary Fig. 7C).

AAV-TT and AAV9 reduce astrocytosis and lysosomal burden in the brain of MPSIIIC mice

Astrocytosis was observed in the thalamus of MPSIIIC mice with non-significant reductions of GFAP (Fig. 7G and H) in both AAV9 and AAV-TT treated groups; no differences were observed in GFAP-positive astrocytes between MPSIIIC and both treated groups in the external capsule (Supplementary Fig. 8A), caudate putamen (Supplementary Fig. 8B), amygdala (Supplementary Fig. 8C) and the cortex (Supplementary Fig. 8D). Levels of LAMP2 lysosomal storage were significantly decreased by both vectors ($P < 0.01$) in the caudate putamen, an area close to the injection site [effect of treatment, $F(3,11) = 16.52$, $P < 0.001$] (Fig. 7I and J). A similar trend was observed in areas distant from the injection site including the external capsule (Supplementary Fig. 9A) and cortex (Supplementary Fig. 9D) and less so in the thalamus (Supplementary Fig. 9B) and amygdala (Supplementary Fig. 9C).

AAV-TT corrects neuroinflammation over AAV9 in the caudate putamen and amygdala of MPSIIIC mice

Immunohistochemical analysis of the brain showed a better correction of inflammation in terms of the number of isolectin B4-positive microglial cells in AAV-TT than AAV9 treated ($P < 0.05$) mice in the caudate putamen [effect of treatment, $F(3,12) = 88.27$, $P < 0.0001$] (Fig. 7K and L) and in the amygdala [effect of treatment, $F(3,12) = 264$, $P < 0.0001$] (Supplementary Fig. 10C). AAV-TT reduced inflammation ($P < 0.001$) similarly to AAV9 ($P < 0.05$) in the cortex [effect of treatment, $F(3,12) = 92.8$, $P < 0.0001$] (Supplementary Fig. 10D); with no improvements in the hippocampus (Supplementary Fig. 10A), thalamus (Supplementary Fig. 10B) and amygdala (Supplementary Fig. 10C).

Figure 7 Continued

microscopy of LAMP2 stained brain sections in wild-type ($n = 4$), untreated MPSIIIC ($n = 3$), AAV9 ($n = 4$) and AAV-TT ($n = 4$) treated MPSIIIC mice shows reduction in lysosomal LAMP2 staining in the caudate putamen in treated MPSIIIC mice. (**K** and **L**) Confocal microscopy of ILB4 stained brain sections in wild-type ($n = 4$), untreated MPSIIIC ($n = 4$), AAV9 ($n = 4$) and AAV-TT ($n = 4$) treated MPSIIIC mice shows improvement in neuroinflammation in the caudate putamen in AAV-TT-HGSNAT treated mice. ANOVA followed by Tukey's *post hoc* multiple comparison test. Data are mean ± SEM; *$P < 0.05$; **$P < 0.01$; ***$P < 0.001$; ****$P < 0.0001$. Scale bar = 50 μm.

Discussion

We used an alternative capsid design approach to generate a variant of AAV2, which is closely related to natural variants that presumably have evolved to efficiently infect human tissues. Intriguingly, when injected in rodents, vectors based on this new capsid show strong tropism for the CNS, including photoreceptors in the eye, rather than for peripheral organ systems, which may be due to changes in the receptor footprint (Asokan *et al.*, 2010; Drouin and Agbandje-McKenna, 2013). One of the most notable changes is the abolished HSPG binding site (Wu *et al.*, 2000; Grifman *et al.*, 2001; Kern *et al.*, 2003; Opie *et al.*, 2003), which steers the AAV-TT capsid away from its tissue culture adapted tropism features and contributes to an increased spread in the CNS *in vivo*. In general, it is thought that high expression levels of HSPG on cell surfaces and extracellular matrix leads to reduced spread and sequestration of AAV2 in 'off target' tissues (Perabo *et al.*, 2006). In the CNS particularly, it has been shown that high affinity for HSPG is detrimental for the spread of transduction by AAV2 (Mastakov *et al.*, 2002; Kanaan *et al.*, 2017). However, preliminary experiments indicate that mutation of the HSPG binding site in AAV2 (R585S and R588S) increases transduction spread and efficiency compared to wild-type AAV2 but to a lower extent than observed for AAV-TT, arguing that additional amino acid changes contribute to the observed phenotype (data not shown). The combined effect of all amino acid replacements is likely to contribute to the increased thermal stability observed for AAV-TT as the difference in stability between AAV-TT and AAV2 is larger than the previously described increase in an AAV2-HSPG null variant, which harbours mutations at positions 585 and 588 (Pacouret *et al.*, 2017). However, the mechanistic link between enhanced capsid stability and increased transduction ability is not entirely understood; primary differences between the capsid variants in various aspects of vector biology, ranging from uptake to genome release in the nucleus, could potentially contribute to the observed differences in transduction efficacy.

Given the encouraging results achieved in AAV2/AAV-TT comparative biodistribution studies, we assessed the efficacy of AAV-TT in correcting neurological deficits in the mouse model of MPSIIIC by comparing it to preferred neurological serotypes. Preparatory GFP distribution studies suggested that at the indicated dose, AAV9 yields very high transduction of cells in localized areas and is not well distributed. In contrast, AAV-TT has less intense levels of staining with a larger proportion of neurons throughout the brain transduced. In adult rodents, neurons are the major cell type transduced with all vectors within both the white and grey matter (Herculano-Houzel, 2014), in keeping with data from AAV9 and AAVrh10 (Cearley and Wolfe, 2006).

It should be noted that AAV-TT and AAVrh10 were affinity-purified and therefore contained a higher number of empty capsids compared to AAV9, which was purified using density gradient centrifugation. The previously described role for empty capsids as decoy for AAV-specific antibodies is unlikely to play a role in the brain given the fact that we could not even detect AAV-specific antibodies after treatment (Mingozzi *et al.*, 2013). However, empty capsids could potentially compete for receptor binding and uptake thereby putting AAV-TT and AAVrh10 at a disadvantage compared to AAV9. Nevertheless, our results show that AAV-TT performed better than AAV9 in the biodistribution studies and was more efficient in correcting the disease in MPSIIIC mice.

Both short-term and long-term data from MPSIIIC mice showed supra-physiological enzyme levels in areas close to the injection site, a distribution pattern seen in other preclinical studies using AAV vectors to treat MPSIIIA (Winner *et al.*, 2016) or MPSIIIB (Fu *et al.*, 2002). Importantly, the treatment did not elicit an antibody response in the brains of MPSIIIC mice.

Although the neuropathology of the brain was corrected in only some regions, we were able to achieve correction of hyperactive behaviour and working memory in AAV-TT treated mice over AAV9 treated mice. It is unclear which brain area is responsible for hyperactivity in MPS, however, the frontostriatal pathway has been implicated in ADHD (Cubillo *et al.*, 2012), as it is involved in control of impulsivity, locomotion, affect, attention and emotion (Takamatsu *et al.*, 2015). This pathway connects the cortex, striatum and thalamus (Morris *et al.*, 2016), areas in which we have observed improvement in LAMP2, GFAP and ILB4 levels with AAV-TT treatment. Hyperactivity could also be a circadian effect controlled from the suprachiasmiatic nucleus as we have hypothesized earlier (Canal *et al.*, 2010), or from areas projecting from the suprachiasmiatic nucleus such as the thalamus (Schwartz *et al.*, 2011). The Y-maze is a widely used test measuring working memory and has been used to study hippocampal function as performance of rodents in this test is disrupted by hippocampal lesions (Rawlins and Olton, 1982; Hock and Bunsey, 1998). The results obtained from the Y-maze test correlate with GFP expression data showing hippocampal vector expression and suggest that effectively transducing these areas can restore hippocampal based learning.

HS has been implicated for its role in neuroinflammation (Zhang *et al.*, 2014), interestingly, AAV-TT treatment improved both HS sulphation patterning and neuroinflammation over AAV9 in several areas. We hypothesize that the sulphation patterning of HS may contribute to neuroinflammation in MPSIIIC potentially resulting in subsequent behavioural abnormalities. These data are consistent with previous findings that suggest that restoring sulphation patterning of HS and reducing inflammation may be key in improving behavioural outcomes in MPSIII (Sergijenko *et al.*, 2013).

G_{M2} and G_{M3} gangliosides have a still undefined role in MPSIIIC neuropathology, and respond differentially to AAV treatment. It has been previously reported that G_{M2}

and G_{M3} gangliosides showed only modest levels of co-localization by both region and subcellular compartment in the brains of MPSIII mice (McGlynn *et al.*, 2004; Martins *et al.*, 2015) with storage also observed in the medial entorhinal cortex in MPSIIIB mice (Ryazantsev *et al.*, 2007; Ohmi *et al.*, 2011). This suggests that different pathological mechanisms underlie storage of G_{M2} and G_{M3} gangliosides in MPSIIIC potentially explaining why they respond differently to restoration of the primary HGSNAT deficiency by AAV-mediated gene correction.

In a disease with global pathology such as MPSIIIC where the enzyme is not secreted and thus cannot cross-correct other cells, maximum cell transduction is required. A similar AAV-based approach has been developed in the non-cross correctable neurological disease CLN3, resulting in some disease correction, although neonatal delivery of AAV is often much more effective than delivery to adult mice (Sondhi *et al.*, 2014). Notably an intravenous AAV9 approach in CLN3 was only partly effective, underlining the difficulty of treating non-cross correctable neurological diseases (Bosch *et al.*, 2016).

Our data for the first time show that the neurological non cross-correctable lysosomal disease MPSIIIC can be treated via AAV-mediated gene therapy suggesting that this may be a therapeutic option for patients.

Acknowledgements

A baculovirus expressing AAV2 virus-like particles was generously donated by Sergei Zolotukhin (Department of Pediatrics, University of Florida). We also thank Dr. Nobuo Hanai, Dr. Akiko Furuya and Kyowa Hakko Kirin Co., Ltd. for a generous gift of monoclonal antibodies against G_{M2} ganglioside.

Funding

R.R.A. received funding from European Union Horizon 2020 (grant No. 66691), RP Fighting Blindness, UK (GR576). R.R.A. is partially supported by the NIHR Biomedical Research Centre at Moorfields Eye Hospital. A.A.R. is funded by the UK Medical Research Council (MR/N026101/1), EU Horizon2020; BATCure 666918 and Action Medical Research (GN2485). S.N.W. received funding from MRC grants MR/P026494/1 and MR/N026101/1. T.B. received funding from a Swedish Research Council (ÄR-MH-2016-01997) Starting grant. M.A.-M. and M.L. were supported by a joined MRC grant to King's College London (MC_PC_13065 'A novel platform for adeno-associated virus vectors for gene therapy'). B.W.B. received funding from Jonah's Just Begun and Vaincre les Maladies Lysosomales. E.H. received funding from King's Commercialisation Institute, the Pfizer Rare Disease Consortium and UK Medical Research Council (MR/N022890/1).

Conflict of interest

E.H. is funded by a Rare Disease Consortium Award from Pfizer Inc. to further develop AAV-TT vector technology. A patent #WO2015121501 on 'Adeno-associated virus vector' has been deposited by M.L., E.H. and J.T. M.L. is a consultant to various gene therapy companies. M.L. is an SAB member of Spark Therapeutics.

M.A.-M. is an SAB member for AGTC, StrideBio, Inc., and Voyager Therapeutics, Inc., is a consultant for Intima Biosciences, and has a sponsored research agreement with AGTC and Voyager Therapeutics, Inc. These companies have interest in the development of AAV for gene delivery applications. M.A.-M. is an inventor of AAV patents licensed to various biopharmaceutical companies. M.A.-M. is a co-founder of StrideBio, Inc. This is a biopharmaceutical company with interest in developing AAV vectors for gene delivery application. The MPSIIIC work in this paper has been patented and licenced to Phoenix Nest Inc, in which B.W.B. is a shareholder.

Supplementary material

Supplementary material is available at *Brain* online.

References

Adachi K, Enoki T, Kawano Y, Veraz M, Nakai H. Drawing a high-resolution functional map of adeno-associated virus capsid by massively parallel sequencing. Nat Commun 2014; 5: 3075.

Archer LD, Langford-Smith KJ, Bigger BW, Fildes JE. Mucopolysaccharide diseases: a complex interplay between neuroinflammation, microglial activation and adaptive immunity. J Inherit Metab Dis 2014; 37: 1–12.

Asokan A, Conway JC, Phillips JL, Li C, Hegge J, Sinnott R, et al. Reengineering a receptor footprint of adeno-associated virus enables selective and systemic gene transfer to muscle. Nat Biotech 2010; 28: 79–82.

Bainbridge JWB, Mehat MS, Sundaram V, Robbie SJ, Barker SE, Ripamonti C, et al. Long-term effect of gene therapy on Leber's congenital amaurosis. N Engl J Med 2015; 372: 1887–97.

Bennett A, Patel S, Mietzsch M, Jose A, Lins-Austin B, Yu JC, et al. Thermal stability as a determinant of AAV serotype identity. Mol Ther Methods Clin Dev 2017; 6: 171–82.

Bevan AK, Duque S, Foust KD, Morales PR, Braun L, Schmelzer L, et al. Systemic gene delivery in large species for targeting spinal cord, brain, and peripheral tissues for pediatric disorders. Mol Ther 2011; 19: 1971–80.

Biasini M, Bienert S, Waterhouse A, Arnold K, Studer G, Schmidt T, et al. SWISS-MODEL: modelling protein tertiary and quaternary structure using evolutionary information. Nucleic Acids Res 2014; 42: W252–8.

Bosch ME, Aldrich A, Fallet R, Odvody J, Burkovetskaya M, Schuberth K, et al. Self-complementary AAV9 gene delivery partially corrects pathology associated with juvenile neuronal ceroid lipofuscinosis (CLN3). J Neurosci 2016; 36: 9669–82.

Boye SL, Bennett A, Scalabrino ML, McCullough KT, Van Vliet K, Choudhury S, et al. Impact of heparan sulfate binding on transduction of retina by recombinant adeno-associated virus vectors. J Virol 2016; 90: 4215–31.

Burger C, Gorbatyuk OS, Velardo MJ, Peden CS, Williams P, Zolotukhin S, et al. Recombinant AAV viral vectors pseudotyped with viral capsids from serotypes 1, 2, and 5 display differential efficiency and cell tropism after delivery to different regions of the central nervous system. Mol Ther 2004; 10: 302–17.

Canal MM, Wilkinson FL, Cooper JD, Wraith JE, Wynn R, Bigger BW. Circadian rhythm and suprachiasmatic nucleus alterations in the mouse model of mucopolysaccharidosis IIIB. Behav Brain Res 2010; 209: 212–20.

Carrillo-Tripp M, Shepherd CM, Borelli IA, Venkataraman S, Lander G, Natarajan P, et al. VIPERdb2: an enhanced and web API enabled relational database for structural virology. Nucleic Acids Res 2009; 37: D436–42.

Cearley CN, Wolfe JH. Transduction characteristics of adeno-associated virus vectors expressing cap serotypes 7, 8, 9, and Rh10 in the mouse brain. Mol Ther 2006; 13: 528–37.

Chen C-L, Jensen RL, Schnepp BC, Connell MJ, Shell R, Sferra TJ, et al. Molecular characterization of adeno-associated viruses infecting children. J Virol 2005; 79: 14781–92.

Chen YH, Chang M, Davidson BL. Molecular signatures of disease brain endothelia provide new sites for CNS-directed enzyme therapy. Nat Med 2009; 15: 1215–18.

Cubillo A, Halari R, Smith A, Taylor E, Rubia K. A review of fronto-striatal and fronto-cortical brain abnormalities in children and adults with Attention Deficit Hyperactivity Disorder (ADHD) and new evidence for dysfunction in adults with ADHD during motivation and attention. Cortex 2012; 48: 194–215.

Deacon RMJ, Bannerman DM, Kirby BP, Croucher A, Rawlins JNP. Effects of cytotoxic hippocampal lesions in mice on a cognitive test battery. Behav Brain Res 2002; 133: 57–68.

Drouin LM, Agbandje-McKenna M. Adeno-associated virus structural biology as a tool in vector development. Future Virol 2013; 8: 1183–99.

Durand S, Feldhammer M, Bonneil É, Thibault P, Pshezhetsky AV. Analysis of the biogenesis of heparan sulfate acetyl-coA: α-glucosaminide N-acetyltransferase provides insights into the mechanism underlying its complete deficiency in mucopolysaccharidosis IIIC. J Biol Chem 2010; 285: 31233–42.

Ellinwood NM, Ausseil J, Desmaris N, Bigou S, Liu S, Jens JK, et al. Safe, efficient, and reproducible gene therapy of the brain in the dog models of Sanfilippo and Hurler syndromes. Mol Ther 2011; 19: 251–59.

Foust KD, Nurre E, Montgomery CL, Hernandez A, Chan CM, Kaspar BK. Intravascular AAV9 preferentially targets neonatal neurons and adult astrocytes. Nat Biotech 2009; 27: 59.

Fu H, Samulski RJ, McCown TJ, Picornell YJ, Fletcher D, Muenzer J. Neurological correction of lysosomal storage in a mucopolysaccharidosis IIIB mouse model by adeno-associated virus-mediated gene delivery. Mol Ther 2002; 5: 42–9.

Gao G-P, Alvira MR, Wang L, Calcedo R, Johnston J, Wilson JM. Novel adeno-associated viruses from rhesus monkeys as vectors for human gene therapy. Proc Natl Acad Sci USA 2002; 99: 11854–59.

Gao G, Vandenberghe LH, Alvira MR, Lu Y, Calcedo R, Zhou X, et al. Clades of adeno-associated viruses are widely disseminated in human tissues. J Virol 2004; 78: 6381–88.

Georgiadis A, Duran Y, Ribeiro J, Abelleira-Hervas L, Robbie SJ, Sunkel-Laing B, et al. Development of an optimized AAV2/5 gene therapy vector for Leber congenital amaurosis owing to defects in RPE65. Gene Ther 2016; 23: 857–62.

Grifman M, Trepel M, Speece P, Gilbert LB, Arap W, Pasqualini R, et al. Incorporation of tumor-targeting peptides into recombinant adeno-associated virus capsids. Mol Ther 2001; 3: 964–75.

Gurda BL, DiMattia MA, Miller EB, Bennett A, McKenna R, Weichert WS, et al. Capsid antibodies to different adeno-associated virus serotypes bind common regions. J Virol 2013; 87: 9111–24.

Herculano-Houzel S. The glia/neuron ratio: how it varies uniformly across brain structures and species and what that means for brain physiology and evolution. Glia 2014; 62: 1377–91.

Hock BJJ, Bunsey MD. Differential effects of dorsal and ventral hippocampal lesions. J Neurosci 1998; 18: 7027–32.

Holley RJ, Ellison SM, Fil D, O'Leary C, McDermott J, Senthivel N, et al. Macrophage enzyme and reduced inflammation drive brain correction of mucopolysaccharidosis IIIB by stem cell gene therapy. Brain 2018; 141: 99–116.

Hughes RN. The value of spontaneous alternation behavior (SAB) as a test of retention in pharmacological investigations of memory. Neurosci Biobehav Rev 2004; 28: 497–505.

Kanaan NM, Sellnow RC, Boye SL, Coberly B, Bennett A, Agbandje-McKenna M, et al. Rationally engineered AAV capsids improve transduction and volumetric spread in the CNS. Mol Ther Nucleic Acids 2017; 8: 184–97.

Kern A, Schmidt K, Leder C, Müller OJ, Wobus CE, Bettinger K, et al. Identification of a heparin-binding motif on adeno-associated virus type 2 capsids. J Virol 2003; 77: 11072–81.

Kim J-Y, Ash RT, Ceballos-Diaz C, Levites Y, Golde TE, Smirnakis SM, et al. Viral transduction of the neonatal brain delivers controllable genetic mosaicism for visualizing and manipulating neuronal circuits *in vivo*. Eur J Neurosci 2013; 37: 1203–20.

Klein RL, Dayton RD, Tatom JB, Henderson KM, Henning PP. AAV8, 9, Rh10, Rh43 vector gene transfer in the rat brain: effects of serotype, promoter and purification method. Mol Ther 2008; 16: 89–96.

Klein RL, Dayton RD, Leidenheimer NJ, Jansen K, Golde TE, Zweig RM. Efficient neuronal gene transfer with AAV8 leads to neurotoxic levels of tau or green fluorescent proteins. Mol Ther 2006; 13: 517–27.

Kotterman MA, Schaffer DV. Engineering adeno-associated viruses for clinical gene therapy. Nature Rev Genet 2014; 15: 445–51.

Langford-Smith A, Langford-Smith KJ, Jones SA, Wynn RF, Wraith JE, Wilkinson FL, et al. Female mucopolysaccharidosis IIIA mice exhibit hyperactivity and a reduced sense of danger in the open field test. PLoS One 2011; 6: e25717.

Lisowski L, Dane AP, Chu K, Zhang Y, Cunningham SC, Wilson EM, et al. Selection and evaluation of clinically relevant AAV variants in a xenograft liver model. Nature 2014; 506: 382–86.

Martins C, Hulkova H, Dridi L, Dormoy-Raclet V, Grigoryeva L, Choi Y, et al. Neuroinflammation, mitochondrial defects and neurodegeneration in mucopolysaccharidosis III type C mouse model. Brain 2015; 138 (Pt 2): 336–55.

Mastakov MY, Baer K, Kotin RM, During MJ. Recombinant adeno-associated virus serotypes 2- and 5-mediated gene transfer in the mammalian brain: quantitative analysis of heparin co-infusion. Mol Ther 2002; 5: 371–80.

McGlynn R, Dobrenis K, Walkley SU. Differential subcellular localization of cholesterol, gangliosides, and glycosaminoglycans in murine models of mucopolysaccharide storage disorders. J Comp Neurol 2004; 480: 415–26.

Mendell JR, Al-Zaidy S, Shell R, Arnold WD, Rodino-Klapac LR, Prior TW, et al. Single-dose gene-replacement therapy for Spinal Muscular Atrophy. N Engl J Med 2017; 377: 1713–22.

Mingozzi F, Anguela XM, Pavani G, Chen Y, Davidson RJ, Hui DJ, et al. Overcoming preexisting humoral immunity to AAV using capsid decoys. Sci Transl Med 2013; 5: 194ra92.

Morris LS, Kundu P, Dowell N, Mechelmans DJ, Favre P, Irvine MA, et al. Fronto-striatal organization: defining functional and microstructural substrates of behavioural flexibility. Cortex 2016; 74: 118–33.

Müller OJ, Kaul F, Weitzman MD, Pasqualini R, Arap W, Kleinschmidt JA, et al. Random peptide libraries displayed on adeno-associated virus to select for targeted gene therapy vectors. Nat Biotech 2003; 21: 1040–6.

Nathwani AC, Reiss UM, Tuddenham EGD, Rosales C, Chowdary P, McIntosh J, et al. Long-term safety and efficacy of factor IX gene therapy in hemophilia B. N Engl J Med 2014; 371: 1994–2004.

Nguyen JB, Sanchez-Pernaute R, Cunningham J, Bankiewicz KS. Convection-enhanced delivery of AAV-2 combined with heparin increases TK gene transfer in the rat brain. Neuroreport 2001; 12: 1961–4.

O'Leary C, Desbonnet L, Clarke N, Petit E, Tighe O, Lai D, et al. Phenotypic effects of maternal immune activation and early

postnatal milieu in mice mutant for the schizophrenia risk gene neuregulin-1. Neuroscience 2014; 277: 294–305.

Ohmi K, Zhao HZ, Neufeld EF. Defects in the medial entorhinal cortex and dentate gyrus in the mouse model of Sanfilippo syndrome type B. PLoS One 2011; 6: e27461.

Opie SR, Warrington JKH, Agbandje-McKenna M, Zolotukhin S, Muzyczka N. Identification of amino acid residues in the capsid proteins of adeno-associated virus type 2 that contribute to heparan sulfate proteoglycan binding. J Virol 2003; 77: 6995–7006.

Pacouret S, Bouzelha M, Shelke R, Andres-Mateos E, Xiao R, Maurer A, et al. AAV-ID: a rapid and robust assay for batch-to-batch consistency evaluation of AAV preparations. Mol Ther 2017; 25: 1375–86.

Perabo L, Goldnau D, White K, Endell J, Boucas J, Humme S, et al. Heparan sulfate proteoglycan binding properties of adeno-associated virus retargeting mutants and consequences for their in vivo tropism. J Virol 2006; 80: 7265–9.

Rahim AA, Wong AM, Ahmadi S, Hoefer K, Buckley SMK, Hughes DA, et al. In utero administration of Ad5 and AAV pseudotypes to the fetal brain leads to efficient, widespread and long-term gene expression. Gene Ther 2012; 19: 936–46.

Rawlins JNP, Olton DS. The septo-hippocampal system and cognitive mapping. Behav Brain Res 1982; 5: 331–58.

Rayaprolu V, Kruse S, Kant R, Venkatakrishnan B, Movahed N, Brooke D, et al. Comparative analysis of adeno-associated virus capsid stability and dynamics. J Virol 2013; 87: 13150–60.

Ripamonti C, Henning GB, Robbie SJ, Sundaram V, van den Born LI, Casteels I, et al. Spectral sensitivity measurements reveal partial success in restoring missing rod function with gene therapy. J Vis 2015; 15: 20.

Ruijter GJ, Valstar MJ, van de Kamp JM, van der Helm RM, Durand S, van Diggelen OP, et al. Clinical and genetic spectrum of Sanfilippo type C (MPS IIIC) disease in The Netherlands. Mol Genet Metab 2008; 93: 104–11.

Russell S, Bennett J, Wellman JA, Chung DC, Yu Z-F, Tillman A, et al. Efficacy and safety of voretigene neparvovec (AAV2-hRPE65v2) in patients with RPE65-mediated inherited retinal dystrophy: a randomised, controlled, open-label, phase 3 trial. Lancet 2017; 390: 849–60.

Ryazantsev S, Yu WH, Zhao HZ, Neufeld EF, Ohmi K. Lysosomal accumulation of SCMAS (subunit c of mitochondrial ATP synthase) in neurons of the mouse model of mucopolysaccharidosis III B. Mol Genet Metab 2007; 90: 393–401.

Salegio EA, Samaranch L, Kells AP, Mittermeyer G, San Sebastian W, Zhou S, et al. Axonal transport of adeno-associated viral vectors is serotype-dependent. Gene Ther 2013; 20: 348–52.

Schwartz MD, Urbanski HF, Nunez AA, Smale L. Projections of the suprachiasmatic nucleus and ventral subparaventricular zone in the Nile grass rat (Arvicanthis niloticus). Brain Res 2011; 1367: 146–61.

Sergijenko A, Langford-Smith A, Liao AY, Pickford CE, McDermott J, Nowinski G, et al. Myeloid/microglial driven autologous hematopoietic stem cell gene therapy corrects a neuronopathic lysosomal disease. Mol Ther 2013; 21: 1938–49.

Seyrantepe V, Canuel M, Carpentier S, Landry K, Durand S, Liang F, et al. Mice deficient in Neu4 sialidase exhibit abnormal ganglioside catabolism and lysosomal storage. Hum Mol Genet 2008; 17: 1556–68.

Shen S, Horowitz ED, Troupes AN, Brown SM, Pulicherla N, Samulski RJ, et al. Engraftment of a galactose receptor footprint onto adeno-associated viral capsids improves transduction efficiency. J Biol Chem 2013; 288: 28814–23.

Sondhi D, Scott EC, Chen A, Hackett NR, Wong AM, Kubiak A, et al. Partial correction of the CNS lysosomal storage defect in a mouse model of juvenile neuronal ceroid lipofuscinosis by neonatal CNS administration of an adeno-associated virus serotype rh.10 vector expressing the human CLN3 gene. Hum Gene Ther 2014; 25: 223–39.

Sparks Therapeutics. Spark Therapeutics presents updated preliminary data from hemophilia B phase 1/2 trial suggesting consistent and sustained levels of factor IX activity at the Hemostasis and Thrombosis Research Society (HTRS) 2017 Scientific Symposium. Press Release, 2017.

Summerford C, Samulski RJ. Membrane-associated heparan sulfate proteoglycan is a receptor for adeno-associated virus type 2 virions. J Virol 1998; 72: 1438–45.

Takamatsu Y, Hagino Y, Sato A, Takahashi T, Nagasawa SY, Kubo Y, et al. Improvement of learning and increase in dopamine level in the frontal cortex by methylphenidate in mice lacking dopamine transporter. Curr Mol Med 2015; 15: 245–52.

Tardieu M, Zerah M, Husson B, de Bournonville S, Deiva K, Adamsbaum C, et al. Intracerebral administration of adeno-associated viral vector serotype rh.10 carrying human SGSH and SUMF1 cDNAs in children with mucopolysaccharidosis type IIIA disease: results of a phase I/II trial. Hum Gene Ther 2014; 25: 506–16.

Tardieu M, Zerah M, Gougeon ML, Ausseil J, de Bournonville S, Husson B, et al. Intracerebral gene therapy in children with mucopolysaccharidosis type IIIB syndrome: an uncontrolled phase 1/2 clinical trial. Lancet Neurol 2017; 16: 712–20.

Tervo DG, Hwang BY, Viswanathan S, Gaj T, Lavzin M, Ritola KD, et al. A designer AAV variant permits efficient retrograde access to projection neurons. Neuron 2016; 92: 372–82.

Tseng Y-S, Gurda BL, Chipman P, McKenna R, Afione S, Chiorini JA, et al. Adeno-associated virus serotype 1 (AAV1)- and AAV5-antibody complex structures reveal evolutionary commonalities in parvovirus antigenic reactivity. J Virol 2015; 89: 1794–808.

Valstar MJ, Ruijter GJ, van Diggelen OP, Poorthuis BJ, Wijburg FA. Sanfilippo syndrome: a mini-review. J Inherit Metab Dis 2008; 31: 240–52.

Vandenberghe LH, Auricchio A. Novel adeno-associated viral vectors for retinal gene therapy. Gene Ther 2012; 19: 162–68.

Wilkinson FL, Holley RJ, Langford-Smith KJ, Badrinath S, Liao A, Langford-Smith A, et al. Neuropathology in mouse models of mucopolysaccharidosis type I, IIIA and IIIB. PLoS One 2012; 7: e35787.

Winner LK, Beard H, Hassiotis S, Lau AA, Luck AJ, Hopwood JJ, et al. A preclinical study evaluating AAVrh10-based gene therapy for Sanfilippo syndrome. Hum Gene Ther 2016; 27: 363–75.

Woodard KT, Liang KJ, Bennett WC, Samulski RJ. Heparan sulfate binding promotes accumulation of intravitreally delivered adeno-associated viral vectors at the retina for enhanced transduction but weakly influences tropism. J Virol 2016; 90: 9878–88.

Worgall S, Sondhi D, Hackett NR, Kosofsky B, Kekatpure MV, Neyzi N, et al. Treatment of late infantile neuronal ceroid lipofuscinosis by CNS administration of a serotype 2 adeno-associated virus expressing CLN2 cDNA. Hum Gene Ther 2008; 19: 463–74.

Wu P, Xiao W, Conlon T, Hughes J, Agbandje-McKenna M, Ferkol T, et al. Mutational analysis of the adeno-associated virus type 2 (AAV2) capsid gene and construction of AAV2 vectors with altered tropism. J Virol 2000; 74: 8635–47.

Zhang X, Wang B, Li JP. Implications of heparan sulfate and heparanase in neuroinflammation. Matrix Biol 2014; 35: 174–81.

Zinn E, Pacouret S, Khaychuk V, Turunen HT, Carvalho LS, Andres-Mateos E, et al. *In silico* reconstruction of the viral evolutionary lineage yields a potent gene therapy vector. Cell Rep 2015; 12: 1056–68.